AGU PUBLICATIONS

Geophysical Research Letters

RESEARCH LETTER
10.1002/2015GL066657

Multiarray rupture imaging of the devastating 2015 Gorkha, Nepal, earthquake sequence

Hao Zhang[1], Suzan van der Lee[1], and Zengxi Ge[2]

[1]Department of Earth and Planetary Sciences, Northwestern University, Evanston, Illinois, USA, [2]School of Earth and Space Sciences, Peking University, Beijing, China

Key Points:
- Slip of the 2015 Gorkha earthquakes was unilateral and tightly confined along-dip
- Our multiarray backprojection method is robust and rapid
- Rupture seems to propagate faster at the upper portion of the slipped MHT segment

Supporting Information:
- Supporting Information S1
- Table S1
- Table S2
- Table S3
- Figure S1
- Figure S2
- Figure S3
- Figure S4
- Figure S5
- Figure S6
- Figure S7
- Figure S8
- Figure S9
- Figure S10

Correspondence to:
H. Zhang,
hzhang@earth.northwestern.edu

Citation:
Zhang, H., S. van der Lee, and Z. Ge (2016), Multiarray rupture imaging of the devastating 2015 Gorkha, Nepal, earthquake sequence, *Geophys. Res. Lett.*, *43*, 584–591, doi:10.1002/2015GL066657.

Received 20 OCT 2015
Accepted 23 DEC 2015
Accepted article online 29 DEC 2015
Published online 20 JAN 2016

Abstract A rapid, robust multiarray backprojection method was applied to image the rupture pattern of the 2015 Gorkha, Nepal M_w7.8 main shock and its M_w7.3 aftershock. Backprojected teleseismic *P* wave trains from three regional seismic arrays in Europe, Australia, and Alaska show that both earthquakes ruptured unilaterally and primarily eastward, with rupture speeds potentially decreasing with depth. The rupture of the main shock first extended ESEward at ~3.5 km/s over ~120 km, with later rupture propagation further downdip on the eastern segment at ~2.1 km/s. The aftershock ruptured the fault SE of the main shock's ruptured plane. It began to rupture updipward for ~20 km at a speed around 1.2 km/s, then it may have accelerated to 3.5 km/s for the next 50 km. The apparent depth-dependent rupture speeds of the two earthquakes may be caused by along-dip heterogeneities in fault strength, with a higher stress concentration on the updip part of the Nepalese Main Himalayan Thrust.

1. Introduction

On 25 April 2015 at 06:11:26 UTC a devastating M_w7.8 earthquake struck about 80 km northwest of the Nepalese capital Kathmandu, destroying numerous buildings and killing many thousands of people (U.S. Geological Survey (USGS), http://earthquake.usgs.gov/earthquakes/eventpage/us20002926#general_summary). The hypocenter of the earthquake is located at ((28.230°N, 84.731°E) ± 7.2 km, 8.2 km ± 2.9 km) (USGS). In view of the ~20 mm/yr northward convergence between the Indian plate and the Tibetan plateau [*Bilham et al.*, 1999], the nodal plane with strike 295°, dip 11°, and rake 108° from the USGS centroid moment tensor (http://earthquake.usgs.gov/earthquakes/eventpage/us20002926#scientific_tensor:us_us_20002926_mwc) most likely represents the fault plane of the 2015 earthquake. Within 27 days of the earthquake, a sequence of aftershocks occurred in a region ~150 km long and ~80 km wide (National Earthquake Information Center) (Figure 1). Two large aftershocks in this sequence had magnitudes of 6.7 and 6.8, which, respectively, occurred ~30 and ~140 km southeast of the main shock's epicenter. The largest, M_w7.3 aftershock occurred on the 28th day after the main shock, just east of the region outlined by the preceding aftershocks and 146 km SSE of the epicenter of the main shock. This aftershock was followed by a M_w6.2 aftershock, ~50 km southeast of the epicenter of the M_w7.3 aftershock. The high similarity of the focal mechanisms among these four largest aftershocks and the main shock strongly suggests that these events all ruptured the Main Himalayan Thrust (MHT; Figure 1).

Before the 2015 earthquake, fault patches of the MHT in Nepal seem to have ruptured increasingly westward in 1255 [*Sapkota et al.*, 2013; *Bollinger et al.*, 2014], 1344 [*Grandin et al.*, 2015], and 1505 [*Ambraseys and Jackson*, 2003] (Figure 1). A M_w7.7 earthquake [*Bilham*, 1995] occurred near the M_w7.3 aftershock in 1833 and may partially overlap the rupture area of the 2015 earthquake. A more recent M_w8.0 earthquake occurred in 1934 in Bihar, Nepal [*Chen and Molnar*, 1977], reactivating the central part of the fault segment ruptured by the 1255 earthquake. *Bilham et al.* [2001] anticipated an earthquake with a magnitude up to 8.3 in the area hit by the 2015 event. That the actual magnitude of the earthquake was smaller (at M_w7.8) than the maximum anticipated implies that parts of faults of the historic 1344 and 1255 earthquakes have not yet slipped in response to built up tectonic stress. These complexities within a simpler large-scale, long-term pattern of tectonic stress build up and transfer demand a detailed study of rupture during the 2015 Nepal earthquake sequence. Such study will apprise the seismic hazard posed by remaining unslipped fault segments,

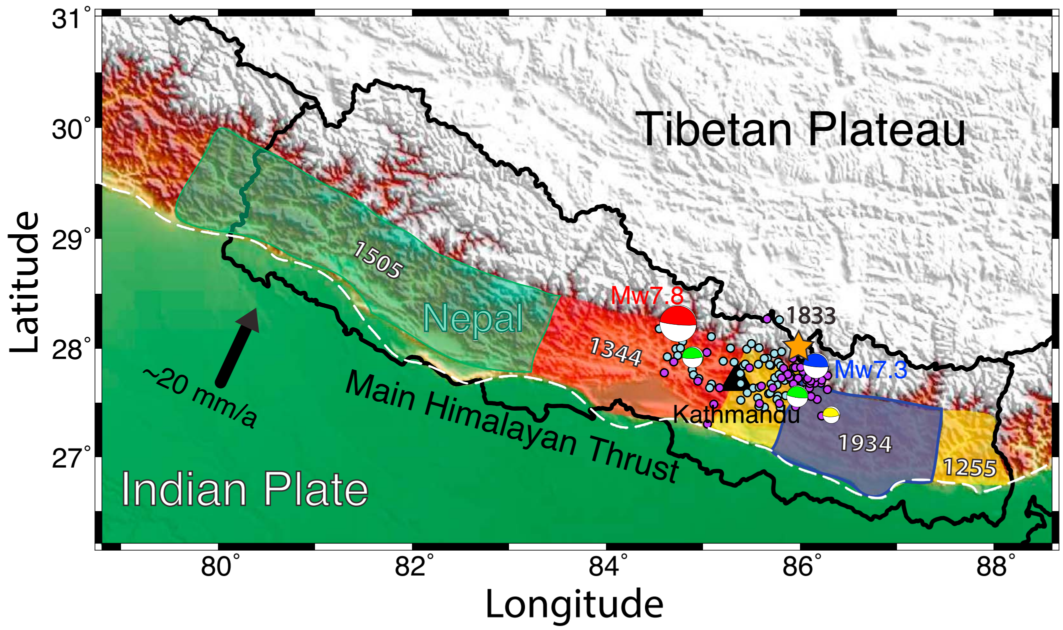

Figure 1. Historic large earthquakes in Nepal and aftershocks of the 2015 Nepal M_w7.8 earthquake. From east to west, three earthquakes sequentially occurred in 1255 (yellow zone), 1344 (red zone), and 1505 (green zone), respectively [*Ambraseys and Jackson*, 2003; *Sapkota et al.*, 2013; *Bollinger et al.*, 2014; *Grandin et al.*, 2015]. An M_w8.0 earthquake (blue zone) the central part of the fault of the 1255 earthquake in 1934 [*Chen and Molnar*, 1977] after a M_w7.7 earthquake (orange star) occurred in 1833 in the northwest [*Bilham*, 1995]. The rupture areas of the ancient earthquakes, especially the 1344 event, could have very large uncertainties. The beach balls represent the focal mechanisms of earthquakes. The red, yellow, and blue ones indicate the 2015 M_w7.8 Gorkha, Nepal earthquake, the May 12, 2015, M_w7.3 aftershock, and the M_w6.2 aftershock, respectively. The green ones depict the M_w 6.7 and 6.8 aftershocks. Light blue and purple circles represent aftershocks of the main shock and the M_w7.3 aftershock, respectively.

which could nucleate other large earthquakes. It is of additional importance to establish rapid robust methods of rupture imaging that can be applied within hours of a main shock and so aid the estimation of aftershock hazard.

The M_w7.8 2015 Nepal earthquake and its largest, M_w7.3 aftershock provide a unique opportunity to study rupture processes of the earthquakes on the MHT and to test a rapid rupture energy imaging method [*Zhang and Ge*, 2010]. Rupture processes of earthquakes are commonly imaged by the backprojection method), first proposed by *Ishii et al.* [2005] and *Krüger and Ohrnberger* [2005]. However, phantom projecting ("swimming") due to trade-offs between path length and rupture duration and along-path smearing of backprojected *P* energy [*Meng et al.*, 2012] can lead to remaining uncertainties and/or artifacts in the rupture model. This issue is addressed here by disallowing *P* energy at a reference seismogram of a central station to contribute to more than one subevent [*Zhang and Ge*, 2010; *Zhang et al.*, 2011] or using a reference window strategy [*Meng et al.*, 2012]. *Xu et al.* [2009] used a global network to mitigate this kind of artifact. However, the global network technique will fail if the coherence of high-frequency waveforms decreases due to depth phases (*pP* and *sP*), rupture directivity, and limited number of stations. The most effective approach to reduce interference from depth phases is to deconvolve the data with the Green's functions during the imaging procedure [*Yagi et al.*, 2012]. However, the calculation of accurate, high-frequency Green's functions is extremely time consuming and requires a thorough level of operator expertise. Alternatively, multiple arrays have been utilized to diminish the smearing artifacts for large earthquakes [*Kiser and Ishii*, 2012; *Zhang et al.*, 2012]. It is very important for rapid, accurate, and robust images of earthquakes' rupture processes to mitigate such imaging artifacts.

Here we apply a rapid multiarray relative *P* wave backprojection method, upgraded from the single-array backprojection method of *Zhang and Ge* [2010], to image the rupture processes of the 2015 Gorkha, Nepal earthquake and its largest aftershock. For both events, teleseismic *P* waves from three large arrays including European seismic network (EU), the Alaska seismic network (AK), and the Australian seismic network (AU) were backprojected. To mitigate ambiguities and potential artifacts, the results from the three single-array backprojections were combined into a multiarray rupture-imaging model. The spatiotemporal resolving power of

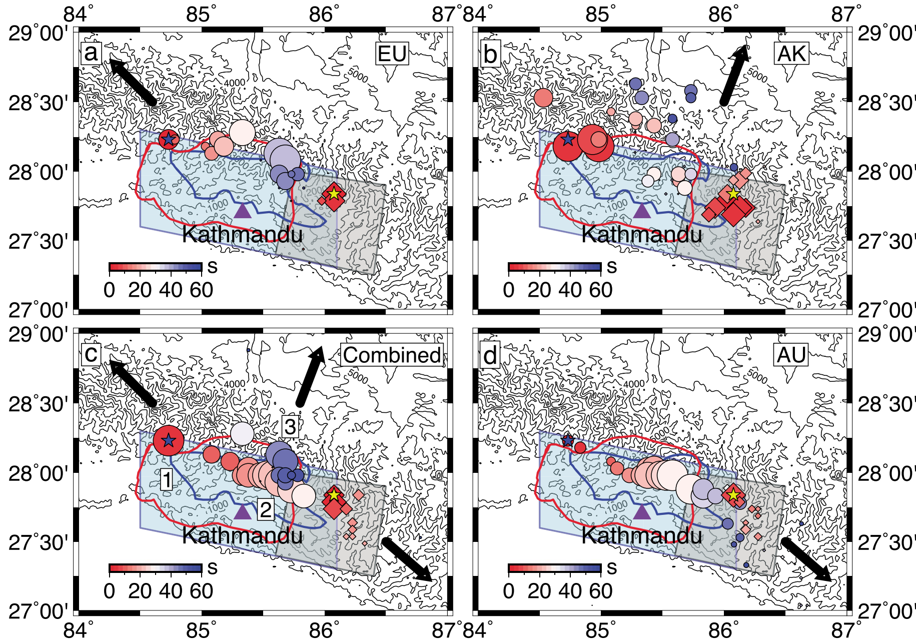

Figure 2. Rupture imaging of the main shock and its largest aftershock from (a) EU, (b) AK, (d) AU, and (c) the combination of the three single arrays. The colored circles and diamonds indicate subevents of the main shock and the M_w7.3 aftershock with area as a function of power. The color bar depicts subevents' rupture times for the two earthquakes. The aftershock zones of the main shock and the aftershock are represented by the light blue and grey quadrangles, respectively. The blue closed, curved line indicates the 1.5 m contour of slip in the geodetic slip model obtained by *Galetzka et al.* [2015], and the red one depicts the 1.5 m contour in the finite fault model derived by *Yagi and Okuwaki* [2015]. The arrows point to the locations of the three arrays. The three energy-releasing peaks of the main shock are labeled with numbers 1, 2, and 3, respectively.

the data is illustrated using six test models. An additional test model was applied to demonstrate the advantage of the multiarray method to diminish artifacts from depth phases and codas. Moreover, the robustness of our rapid multiarray backprojection procedure has been demonstrated by comparing our main shock results, which were obtained within 2 days of the main shock and first posted online on 29 April 2015 [*H. Zhang et al.*, 2015], with other backprojection results [*Avouac et al.*, 2015; *Fan and Shearer*, 2015; *Hutko*, 2015].

2. Data and Methodology

To image the rupture processes of the 2015 Nepal main shock and its largest aftershock rapidly and accurately, we applied the multiarray relative backprojection method [*Zhang et al.*, 2012] using teleseismic *P* waves, before identifying and locating relatively discrete subevents of the main shock. Raw instrumental *P* wave trains from three seismic arrays (EU, AK, and AU) were converted to ground velocity, then band-pass filtered between 0.5 and 2.5 Hz. The first time window is 10 s long for the main shock and 6 s long for the aftershock and begins at the first *P* arrival time. Traces with a signal-to-noise ratio $\left(\mathrm{SNR} = 10 * \log_{10}\frac{\text{Power of signal}}{\text{Power of noise}}\right)$ below 10 and coherence with a reference trace below 0.6 were discarded. This culling left 74 EU stations, 52 AK stations, and 41 AU stations for the main shock (Figure S1 in the supporting information) and 72 EU stations, 75 AK stations, and 42 AU stations for the aftershock (Figure S2). The geometry of these station ensembles is similar for the two events (Figures S1c and S2c). The azimuthal and spatial extents of the AK array are more limited than those of arrays EU and AU (Figure S1 and S2), allowing more smearing of the imaged power; this is further confirmed by the array response function (ARF; Figure S3).

We developed our multiarray backprojection model of the main shock in two steps. At the first step, data at the three arrays were back projected using the single-array method [*Zhang and Ge*, 2010]. For each array, a grid search over the fault plane determines the most likely location of rupture energy release. Because the MHT dips gently, it is reasonable to assume that the main shock ruptured the subhorizontal fault plane of the USGS focal mechanism, which we approximate by a horizontal plane centered at the hypocenter. We gridded this plane into 101 × 101 blocks placed at every 0.05° of both latitude and longitude. Each second, for the first

100 s after the first *P* arrival time, 10 s long *P* wave trains were stacked with the differential slowness expected for each potential subevent on the gridded fault plane. The potential subevent with the maximum power was considered as the actual source of the *P* wave energy in the considered window (Figures 2a, 2b, and 2d). The rupture time of this subevent was then calculated as detailed by *Zhang and Ge* [2010]. In Figure 2, the subevents are plotted as circles (main shock) or diamonds (aftershock), colored by rupture time. The stacked *P* wave train amplitude (power) for each subevent is reflected by the size of the symbols.

The second step was to combine the results inferred by the three arrays by summing their on-fault power distributions at each time step and then to identify subevents. To equalize contribution of the three arrays, the weights of the EU, AK, and AU were set to 0.45, 0.3, and 0.25, respectively, though the effect of these weighting factors is weak. Next, locations and rupture times of the subevents were determined as described above, and the multiarray backprojection result is shown in Figure 2c.

For the aftershock, the same multiarray relative backprojection imaging procedure as applied to the main shock was carried out. However, the gridded source region was centered at the hypocenter of the aftershock ((27.837°N, 86.077°E) $\pm$ 7.4 km, 15 km $\pm$ 1.7 km (provided by USGS)), and the sliding time window had a length of 6 s. Moreover, the weights of the three arrays were set to 0.65, 0.15, and 0.20 respectively. The rupture processes of the aftershock imaged by the three single arrays and their combination are illustrated in Figure 2.

3. Multiarray Backprojection Rupture Models

Figure 2c shows our best backprojected rupture model. This multiarray backprojection model shows that the spatial evolution of subevents of the main shock is greatly consistent with a 292° (WNW) strike and gentle dip of the fault plane. The rupture appears to propagate unilaterally to the ESE over a length of ~120 km in a duration of ~60 s in two main stages (inset b of Figure 4). In the first 30 s, the earthquake ruptures ESEward along strike at a high velocity of 3.5 $\pm$ 0.5 km/s. Next, the downdip part of the fault joins the updip part in generating high-frequency signals and the rupture propagates ESEward during the last 30 s at a slower speed of 2.1 $\pm$ 0.4 km/s. There are three main energy-releasing peaks (Figure 2c and inset a of Figure 4): one near the epicenter, 5 s after the origin time, a second one occurs 90 km ESE of the epicenter at 23 s, and a third one locates just north of the second one, at 43 s.

The largest aftershock, which occurred just east of the main shock rupture plane (Figures 2c and 4), appears to have ruptured unilaterally SSEward, slightly updip, over a length of 70 km within 28 s. The aftershock has a smaller, more compact rupture with a larger along-dip component than the main shock. The along-dip resolving power of 5.5 km (Table S1) would suggest that this aftershock also ruptured in two stages: a southward rupture over a length of 20 km at a low apparent speed of around 1.2 $\pm$ 0.2 km/s, which releases much high-frequency energy, and a SSE extending rupture over a length of ~50 km at a high apparent speed of 3.5 $\pm$ 0.2 km/s. The high energy-releasing peak is located ~5 km south of the aftershock's epicenter.

Intriguingly, the apparently slowly propagating rupture segments of both earthquakes are at similar depths (~15 km), based on USGS hypocenters and even though only one of the quakes nucleated at that depth. These segments are 5 to 10 km deeper than the shallower segments suggesting faster and more purely along-strike rupture propagation. Rupture propagation found for the aftershock has a stronger S component than that for the main shock, which is not inconsistent with the ~12° southward turn of the strike of the MHT.

Also intriguingly, little high-frequency energy seems to have been released in between the first two subevents of the main shock (Figures 2c and 4). High-frequency energy mainly originates from the sudden change of rupture velocity [*Madariaga*, 1977]. This interpretation of our backprojection image would imply that rupture propagated more smoothly at the beginning, before the second subevent. This implication is consistent with the smooth onset of rupture observed in the geodetic imaging rupture model of *Galetzka et al.* [2015].

Our multiarray results are better constrained than our single-array results. Due to the limited azimuthal coverage of any one array, rupture imaging can show artificial "smearing" of rupture energy toward the array along the ray paths [*Kiser and Ishii*, 2012; *Zhang et al.*, 2012]. This is also the case in the imaging results from the narrowest AK array (Figure 2b). The combination of multiple arrays with different azimuths significantly increases the azimuthal coverage of data and thus better resolves the actual sources of rupture energy. Other artifacts could stem from the method's bias toward imaging rupture in the direction of, rather than away from, an array, as the associated Doppler effect may increase the signal-to-noise ratio [*Zhang et al.*, 2012]. An advantage of our multiarray approach is that it images the rupture from different directions, which shows consistency of

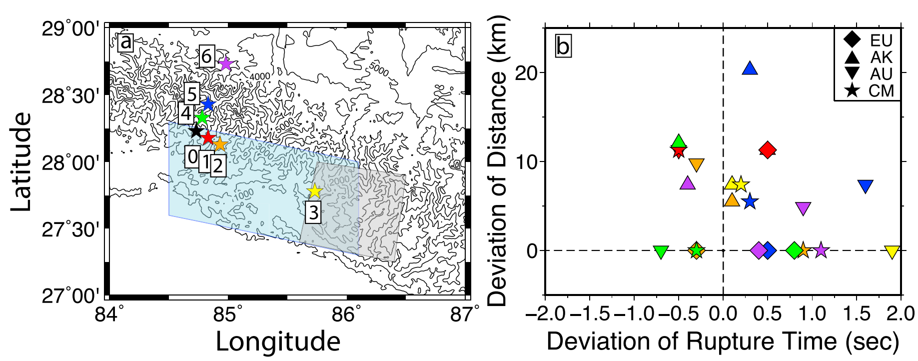

Figure 3. Resolving power of the three single arrays (EU, AK, and AU) and their combination. (a) Locations of the seven sources forming six models listed in Table S1. Models 1–6 are composed of source 0 (black star) at the epicenter and the other source labeled 1–6, respectively. (b) Deviations of location and rupture time from the presetting values for sources 1–6 derived by the three single arrays (EU, diamond; AK, triangle; AU, inverse triangle) and their combination (star). The red, orange, yellow, green, blue, and purple colors indicate sources 1–6 in the left panel, respectively.

the main shock's unilateral ESEward rupture in the backprojected rupture models derived separately from the EU and AU arrays (Figures 2a and 2d), which are in opposite directions. This consistency allows additional confidence in the combined results. In the following section we assess the extent to which these known potential artifacts retain an influence on our best backprojection model.

4. Synthetic Assessment of Backprojection Results

To assess the backprojection results, we synthesized seismograms, using the orthonormal propagator method [*Wang*, 1999], at the three arrays for six two-subevent models as shown in Figure 3a and listed in Table S1. Four of the six models near the epicenter of the main shock could be also applied to test the aftershock's imaging results due to similar configurations of the three arrays and ray paths (Figures S1 and S2). The performance and analyses of these tests are detailed in Text S1. Resolution tests, as illustrated in Figure 3b, show that in general, the data's spatial and temporal resolving power for a range of possible rupture models is within ∼11 km and ∼1 s, respectively. Two of the tested models were misimaged by two single arrays by nearly twice that. The multiarray results are within the former errors for cases, including those where a single array could produce a large error. These errors for both the main shock and aftershock are 11 km and 1 s for along-strike and 5.5 km and 0.5 s for along-dip rupture. Sources of error mainly originate from interferences of depth waves (*pP* and *sP*) generated by the subevents themselves or preceding ones and the array response function (Figures S4–S9).

To quantitatively evaluate the artifacts introduced by depth phases (*pP* and *sP*) and coda waves such as *pPmP* and *sPmP*, we carried out another test with source 0 at the epicenter of the main shock (Figure 3a) and by using the synthetic seismograms at the three arrays and their combination. The backprojection results (Figure S10) show that in all four cases artifacts from backprojecting the depth phases are minor except for the array AU, which shows an artificial large-energy subevent at 2 s. In addition, the coda waves lead to along-path artifacts toward the arrays (Figure S10). However, these artificial subevents all have much less energy than the subevents imaged from the data, indicating a minor interference with the backprojection imaging results. More importantly, the multiarray backprojection results (Table S2) show the least interference from the depth phases and coda waves. This finding suggests that the multiarray relative backprojection method is able to diminish artifacts effectively, thereby providing more robust results than a single-array backprojection.

5. Discussion

Soon after the 2015 M_w7.8 Nepal earthquake, many groups and individuals performed a variety of investigations on this earthquake, resolved complex earthquake properties, and immediately shared the results with the world as listed in Table S3. The finite fault model inverted by *Yagi and Okuwaki* [2015] shows the earthquake unilaterally ruptures a large asperity to the ESE at 3.0 km/s over 140 km in 50 s and causes the maximum slip (7.5 m) 50 km ESE of the epicenter. A geodetic slip model obtained by *Galetzka et al.* [2015] shows the earthquake rupture a fault of 140 km long at 3.3 km/s with the maximum slip of ∼6 m located nearby Kathmandu. Subevents in our multiarray backprojection imaging model seem to mostly be located near the bottom edges of significant slip in these two slip models (Figure 4), as well as other slip models [e.g., *Hayes*, 2015;

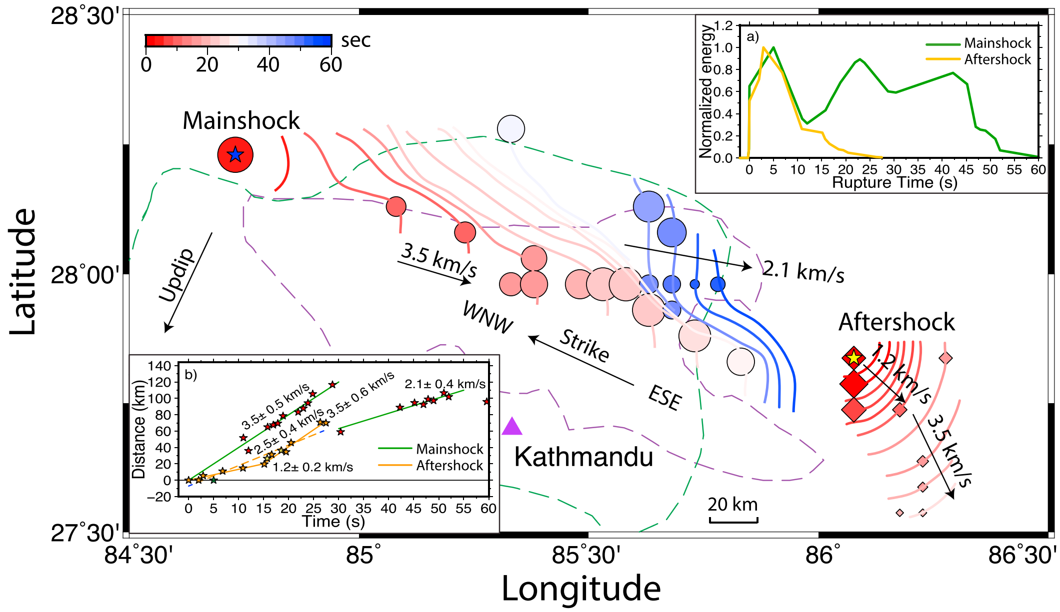

Figure 4. Interpretation on evolution of the rupture front with time for both the main shock and M_w7.3 aftershock. The curved lines represent the rupture fronts as a function of rupture time, which is indicated by the color bar. The circles indicates the high-frequency subevents at the rupture front resolved by the multiarray backprojection method. The purple closed, dashed line indicates the 1.5 m contour of slip in the geodetic slip model obtained by *Galetzka et al.* [2015], while the green one depicts the 1.5 m contour in the finite fault model derived by *Yagi and Okuwaki* [2015]. Inset a: normalized power of the subevents in the multiarray relative backprojection rupture models as a function of rupture time. The green and orange curved lines depict subevents of the main shock and the M_w7.3 aftershock, respectively. Inset b: distances of subevents of the main shock and M_w7.3 aftershock from their own epicenters as a function of rupture time, starting from their own origin times. The green and orange stars indicate the subevents of the main shock and the M_w7.3 aftershock, respectively.

Wang et al., 2015; *Y. Zhang et al.*, 2015]. This observation is similar to the frequency-dependent backprojection images for shallow oceanic subduction zone earthquakes, which has been ascribed by *Lay et al.* [2012], *Yao et al.* [2013], and *Vall'ee and Satriano* [2014] to the size of asperities decreasing as temperature and pressure increase with depth.

Additionally, our backprojection model was determined within 2 days of the earthquake and appears to be largely consistent with other rupture models published since then [*IRIS DMC*, 2011; *Avouac et al.*, 2015; *Fan and Shearer*, 2015], though their estimates of average rupture velocity range from ~2 to ~3 km/s, which is lower than our estimate of rupture velocity during the first 30 s. Some differences between some other backprojection models of the main shock and ours may be caused by the following three factors. First, the relative backprojection method we used diminishes "swimming" artifacts in the backprojection results as shown in Figure S10. Second, the coherence of our data is higher than that of a global data set because we stack only seismograms that pass a culling criterion from one array at a time. Third, artifacts from depth phases *pP* and *sP* and coda waves, originated from Green's functions and radiation pattern, may be more effectively mitigated by our multiazimuthal, large-aperture arrays comprising 187 stations (Figure S10) than by a global network including much fewer stations.

For both the main shock and M_w7.3 aftershock, the speed of rupture propagation could be one to two thirds smaller at the deeper end of the ruptured fault plane than at the shallow end (inset b of Figure 4). Such an interpretation could explain the imaged pattern of both events' subevents as resulting from a two-dimensional rupture front that radiates with a depth-dependent rupture velocity. For the main shock this would mean that the high-frequency subevent at the onset of the second stage, which seems to "jump back" WNWward, essentially signifies the arrival there of the same smooth rupture front that extended rapidly ESEward, except that it took the rupture front longer to get to the second-stage subevent location on the deeper stretch of the fault. The relatively smooth propagation of the initial rupture front at depth appears to continue to propagate slowly even as the onset of stage 2 marks the release of relatively more high-frequency energy (Figure 4).

Rupture speed may be mainly controlled by the initial stress and fault strength [*Zhang and Chen*, 2006]. Their dynamic rupture model suggests that the closer the initial stress approaches the fault strength, the faster the rupture would propagate. This implies that the relatively shallow part of the MHT, at the same depth as the main shock's nucleation depth, experienced higher stress or lower strength than the deeper part. Lower initial stress at depth could be consistent with the inference by *Lay et al.* [2012] that deeper asperities are smaller. Alternatively, our apparent depth-dependent rupture velocity may be a direct result of the depth-dependent asperities inferred by *Lay et al.* [2012], in which smaller asperities imply larger interasperity zones in which rupture propagates more smoothly and slowly. Thus, it is possible that the relatively high rupture velocity at the relatively shallow part of the fault indicates a higher state of stress, a lower fault strength, or larger asperities than on the MHT than on somewhat deeper parts of the fault.

6. Conclusions

The strong consistency of worldwide rupture models for the Gorkha, Nepal earthquake is remarkable [*Avouac et al.*, 2015; *Fan and Shearer*, 2015; *Galetzka et al.*, 2015; *Grandin et al.*, 2015; *Hayes*, 2015; *IRIS DMC*, 2011; *Wang et al.*, 2015; *Yagi and Okuwaki*, 2015; *H. Zhang et al.*, 2015; *Y. Zhang et al.*, 2015] and illustrates the power of continental-scale seismic arrays in the context of seismic hazard assessment. Our multiarray backprojection approach was capable of providing a robust high-frequency rupture model within 2 days of the earthquake. Faster results may be possible for future earthquakes. The multiarray backprojection rupture model presented here shows that the 2015 M_w7.8 Nepal earthquake unilaterally ruptured to the ESE over 120 km within ~60 s and its largest aftershock ruptured SSEward (updipward) over 70 km in a duration of 28 s. Both earthquakes seem to have two stages of rupture. For the main shock, the rupture propagated at a high average speed in the first stage, then extended in the second stage on the downdip portion of the fault at a lower speed. The largest aftershock occurred east of the main shock's rupture plane. The rupture during the aftershock seems to have begun proceeding slowly updipward on the deeper portion of the fault, then may have propagated faster in the second stage on the shallower part of the fault. It is possible that the relatively high rupture velocity at the relatively shallow part of the fault reflects along-dip heterogeneity in stress, strength, structure, or all of these and could indicate a higher state of stress, a lower fault strength, or larger asperities than on the somewhat deeper parts of the Nepalese MHT.

Acknowledgments
We thank the editor Andrew V. Newman and two anonymous reviewers for their constructive comments that helped us to focus and improve the manuscript. We thank Trevor Bollmann, Emily Wolin, and Michael Witek for their valuable comments on earlier versions of this manuscript. H.Z. thanks Edward M. Brooks for his language polishing. SL thanks seismology colleagues at Géoazur and Jean-Paul Ampuero for their inspiring earthquake discussions. We are particularly grateful to Mathilde Vergnolle, Bertrand Delouis, Cecile Cornou, and Yann Klinger, who rapidly and open mindedly collected a variety of helpful information on the Gorkha earthquake, including the here presented backprojection model, into a dedicated web site: https://sites.google.com/site/cellulepostsismique/earthquake-nepal-mw-7-9-april-25-2015. The figures in this manuscript were plotted with Generic Mapping Tools [*Wessel and Smith*, 1995]. Utilized seismic waveform data were downloaded from the IRIS-DMC (http://ds.iris.edu). This research was supported by Northwestern University and Géoazur (Sophia-Antipolis, France), which respectively and generously hosted the first two authors. Z.G. was supported by National Scientific Foundation of China grant 41374045.

References

Ambraseys, N. N., and D. Jackson (2003), A note on early earthquakes in northern India and southern Tibet, *Curr. Sci.*, *84*, 570–582.

Avouac, J.-P., L. Meng, S. Wei, T. Wang, and J.-P. Ampuero (2015), Lower edge of locked Main Himalayan Thrust unzipped by the 2015 Gorkha earthquake, *Nat. Geosci.*, *8*(9), 708–711.

Bilham, R. (1995), Location and magnitude of the 1833 Nepal earthquake and its relation to the rupture zones of contiguous great Himalayan earthquakes, *Current Science*, *69*(2), 101–128.

Bilham, R., K. Larson, J. Freymueller, and Project Idythim members (1999), GPS measurements of present-day convergence across the Nepal Himalaya, *Nature*, *386*, 61–44.

Bilham, R., V. K. Gaur, and P. Molnar (2001), Himalayan seismic hazard, *Science*, *293*, 1442–1444.

Bollinger, L., S. N. Sapkota, P. Tapponnier, Y. Klinger, M. Rizza, J. van der Woerd, D. R. Tiwari, R. Pandey, A. Bitri, and S. Bes de Berc (2014), Estimating the return times of great Himalayan earthquakes in eastern Nepal: Evidence from the Patu and Bardibas strands of the Main Frontal Thrust, *J. Geophys. Res. Solid Earth*, *119*, 7123–7163, doi:10.1002/2014JB010970.

Chen, W. P., and P. Molnar (1977), Seismic moments of major earthquakes and the average rate of slip in central Asia, *J. Geophys. Res.*, *82*(20), 2945–2969.

Fan, W., and P. M. Shearer (2015), Detailed rupture imaging of the 25 April 2015 Nepal earthquake using teleseismic *P* waves, *Geophys. Res. Lett.*, *42*, 7467–7475, doi:10.1002/2015GL064587.

Galetzka, J., et al. (2015), Slip pulse and resonance of the Kathmandu basin during the 2015 Gorkha earthquake, Nepal, *Science*, *349*(6252), 1091–1095.

Grandin, R., M. Vallée, C. Satriano, R. Lacassin, Y. Klinger, M. Simoes, and L. Bollinger (2015), Rupture process of the M_W=7.9 2015 Gorkha earthquake (Nepal): Insights into Himalayan megathrust segmentation, *Geophys. Res. Lett.*, *42*, 8373–8382, doi:10.1002/2015GL066044.

Hayes, G. P., et al. (2015), Rapid Characterization of the 2015 Mw 7.8 Gorkha, Nepal, Earthquake Sequence and Its Seismotectonic Context, *Seismol. Res. Lett.*, *86*(6), 1557–1567.

Hutko, A. (2015), Back projections for MWW 7.9 Nepal. [Available at http://ds.iris.edu/spud/backprojection/9924467, last accessed on May 6th, 2015.]

IRIS DMC (2011), Data Services Products: BackProjection P-wave back-projection rupture imaging, doi:10.17611/DP/9924467.

Ishii, M., P. M. Shearer, H. Houston, and J. E. Vidale (2005), Extent, duration and speed of the 2004 Sumatra-Andaman earthquake imaged by the Hi-Net array, *Nature*, *435*(7044), 933–936.

Kiser, E., and M. Ishii (2012), Combining seismic arrays to image the high-frequency characteristics of large earthquakes, *Geophys. J. Int.*, *188*(3), 1117–1128.

Krüger, F., and M. Ohrnberger (2005), Tracking the rupture of the M_W=9.3 Sumatra earthquake over 1,150 km at teleseismic distance, *Nature*, *435*(7044), 937–939.

Lay, T., H. Kanamori, C. J. Ammon, K. D. Koper, A. R. Hutko, L. Ye, H. Yue, and T. M. Rushing (2012), Depth-varying rupture properties of subduction zone megathrust faults, *J. Geophys. Res.*, *117*, B04311, doi:10.1029/2011JB009133.

Madariaga, R. (1977), High-frequency radiation from crack (stress drop) models of earthquake faulting, *Geophys. J. R. Astron. Soc.*, *51*, 625–651.

Meng, L., J.-P. Ampuero, Y. Luo, W. Wu, and S. Ni (2012), Mitigating artifacts in back-projection source imaging with implications on frequency-dependent properties of the Tohoku-Oki earthquake, *Earth Planets Space*, *64*(12), 1101–1109.

Vall'ee, M., and C. Satriano (2014), Ten year recurrence time between two major earthquakes affecting the same fault segment, *Geophys. Res. Lett.*, *41*, 2312–2318, doi:10.1002/2014GL059465.

Sapkota, S. N., L. Bollinger, Y. Klinger, P. Tapponnier, Y. Gaudemer, and D. Tiwari (2013), Primary surface ruptures of the great Himalayan earthquakes in 1934 and 1255, *Nat. Geosci.*, *6*, 71–76.

Wang, R. (1999), A simple orthonormalization method for stable and efficient computation of Green's functions, *Bull. Seismol. Soc. Am.*, *89*(3), 733–741.

Wang, W., J. Hao, J. He, and Z. Yao (2015), Rupture process of the M_w7. 9 Nepal earthquake April 25, 2015, *Sci. China Earth Sci.*, *58*, 1895–1900.

Wessel, P., and W. H. F. Smith (1995), New version of Generic Mapping Tools released, *Eos Trans. AGU*, *76*, 329.

Xu, Y., K. D. Koper, O. Sufri, L. Zhu, and A. R. Hutko (2009), Rupture imaging of the M_w7.9 12 May 2008 Wenchuan earthquake from back projection of teleseismic P waves, *Geochem. Geophys. Geosyst.*, *10*, Q04006, doi:10.1029/2008GC002335.

Yao, H., P. M. Shearer, and P. Gerstoft (2013), Compressive sensing of frequency-dependent seismic radiation from subduction zone megathrust ruptures, *Proc. Natl. Acad. Sci. U.S.A.*, *110*(12), 4512–4517.

Yagi, Y., A. Nakao, and A. Kasahara (2012), Smooth and rapid slip near the Japan Trench during the 2011 Tohoku-oki earthquake revealed by a hybrid back-projection method, *Earth Planet. Sci. Lett.*, *355*, 94–101.

Yagi, Y., and R. Okuwaki (2015), Integrated seismic source model of the 2015 Gorkha, Nepal, earthquake, *Geophys. Res. Lett.*, *42*, 6229–6235, doi:10.1002/2015GL064995.

Zhang, H., and X. Chen (2006), Dynamic rupture on a planar fault in three-dimensional half-space—II. Validations and numerical experiments, *Geophys. J. Int.*, *167*(2), 917–932.

Zhang, H., J. Chen, and Z. Ge (2012), Multi-fault rupture and successive triggering during the 2012 M_w 8.6 Sumatra offshore earthquake, *Geophys. Res. Lett.*, *39*, L22305, doi:10.1029/2012GL053805.

Zhang, H., and Z. Ge (2010), Tracking the rupture of the 2008 Wenchuan earthquake by using the relative back-projection method, *Bull. Seismol. Soc. Am.*, *100*(5B), 2551–2560.

Zhang, H., Z. Ge, and L. Ding (2011), Three sub-events composing the 2011 off the Pacific coast of Tohoku Earthquake (M_w9.0) inferred from rupture imaging by back-projecting teleseismic P waves, *Earth Planets Space*, *63*(7), 595–598.

Zhang, H., S. van der Lee, and Z. Ge (2015), Backprojection of the P-wave energy from the earthquake analysis for the April 25, 2015 mainshock. [Available at https://sites.google.com/site/cellulepostsismique/earthquake-nepal-mw-7-9-april-25-2015, last accessed on May 6th, 2015.]

Zhang, Y., L. S. Xu, and Y. T. Chen (2015), Rupture process of the 2015 Nepal M_w7.9 earthquake: Fast inversion and preliminary joint inversion, *Chinese J. Geophys.*, *58*(5), 1804–1811.